# Applying tactile sensing with piezoelectric materials for minimally invasive surgery and magnetic-resonance-guided interventions

**A M Hamed**[1]*, **Z T H Tse**[1], **I Young**[2], **B L Davies**[1], and **M Lampérth**[1]
[1]Department of Mechanical Engineering, Imperial College London, London, UK
[2]Department of Electrical Engineering, Imperial College London, London, UK

*The manuscript was received on 9 July 2008 and was accepted after revision for publication on 23 September 2008.*

DOI: 10.1243/09544119JEIM473

**Abstract:** Medical technologies have undergone significant development to overcome the problems inherent in minimally invasive surgery such as inhibited manual dexterity, reduced visual information, and lack of direct touch feedback to make it easier for surgeons to operate. A minimally invasive tool incorporating haptic feedback is being developed to increase the effectiveness of diagnostic procedures by providing force feedback. Magnetic resonance imaging guidance is possible to allow tool localization; however, this engenders the requirement of magnetic resonance compatibility on the device. This paper describes the work done towards developing a sensing device using piezoelectric sensor elements to locate subsurface inclusions in soft substrates, with its magnetic resonance compatibility tested in a 1.5 T scanner. Results show that the position of a hard inclusion can be determined.

**Keywords:** magnetic resonance compatible, minimally invasive surgery, tactile sensing, piezoelectric

## 1 INTRODUCTION

In minimally invasive surgery (MIS), the main premise is to minimize superfluous trauma to the patient as much as possible, thus ensuring that the patient recovery time is much faster and that the potential for surgery-related complications is reduced. To achieve this, the surgical procedure is conducted through the smallest incisions possible using thin-handled instruments inserted into the operating area and classically using an instrument with a camera and light source at its distal end (known as an endoscope) for visualization. The problems associated with this format are that the surgery becomes much more technically demanding, as the surgeon has greatly inhibited visual information, must perform much more complicated manipulations, and loses touch information almost entirely [**1**].

**Corresponding author: Department of Mechanical Engineering, Imperial College London, Exhibition Road, South Kensington, London, SW7 2AZ, UK. email: a.hamed@imperial.ac.uk*

As such, MIS is an intuitive direction for the development of surgical robotics, where the accuracy and repeatability of the devices can be made to overcome the limitations of the surgeon by design. It is also possible to incorporate various forms of sensor that can be used to assess forces generated by interaction with tissues or to examine the structure and properties of the tissue itself. Such robots are becoming more common for use in biopsies, MIS tele-surgery, and laparoscopic and arthroscopic surgeries [**2**].

Significant advantages can be achieved when utilizing an imaging technology for guidance in conjunction with MIS robotics. This combination provides the advantages of both formats and allows the possibility of targeting otherwise hidden tissue locations in the body, and, by use of trajectory planning, tool entry, operation, and extraction can be optimized uniquely for the morphology of each patient. When using image guidance in real time in this way, it is also possible for the system to track both the instruments and the tissues of the body. This is important when operating on mobile pathol-

ogies such as the liver. The increased accuracy of the image-guided procedures has been shown to improve statistically the outcome of surgery as it is less likely that an operation must be repeated or that complications occur owing to surgical inaccuracies [**3**, **4**].

Ultrasound and magnetic resonance imaging (MRI) are most suitable for use in longer-duration image-guided procedures because of the lack of ionizing radiation. However, MRI has several advantages, primarily its ability to distinguish clear boundaries between soft-tissue structures without the need for contrast agents. Additionally, MRI can also be used to produce tomographic images in several planes without needing to reposition the patient. Also, as the scans are programmed sequences, it has the ability to be used in many formats to image brain activity, blood flow, and even chemical composition and stiffness of tissues depending on the information required [**5**]. These advantages have driven the development of mechatronic systems for use with scanners [**6**–**10**].

Despite these apparent advantages, MRI also poses several challenges when designing mechatronic systems owing to its operating principle and physical conformation. The dimensions of the machine restrict the surgeon's access to a patient such that invasive operations are difficult. The presence of a large magnetic field, that is required to be highly homogenous within the magnetic isocentre, and the use of radio frequency (r.f.) radiation produce the necessity for magnetic resonance (MR) compatibility in all tools and devices that are used close to and within the scanner bore. These concepts are defined, first, by ASTM F2503-05 [**11**] to qualify the size of image distortion produced by the device; second, by a signal-to-noise ratio (SNR) test to measure the signal reduction from the MR images after the device has been introduced into the scanner [**12**]; and, third, by the geometrical distortion test to investigate the phase shift and spatial distortion in the image. As such, all devices that are designed for use with MRI must have this as one of their primary design specifications.

A search of the available literature indicates that there have been very few systems developed for MR-compatible force sensing, and currently there are no commercial MR-compatible systems available. Work has been done by Burdet *et al.* [**13**] in developing haptic (force feedback) MR-compatible devices for neuroscience research, and some MR-compatible force sensors have also been developed [**14**–**16**]. Use of optical techniques to avoid interference is common. Another MR-compatible system that features optical encoders is the NeuroArm developed by Sutherland *et al.* [**17**]. This is a robotic system for neurosurgery and incorporates hand controllers with force feedback to feel forces on the tools at the end effectors. An MR-compatible haptic system for measuring forces during needle insertion has been developed by Tse *et al.* [**18**] using piezoresistive force sensors.

Some systems exist for measuring tissue stiffnesses; however, these are not MR compatible and are for use during operations when the target tissue can be located after the necessary incisions have been made [**19**–**22**] or for measuring the forces being applied by the tools on the tissue during operations [**23**, **24**]. To make tissue stiffness measurements on hidden tissue without operation, target area identification and then guidance by an imaging system with good soft-tissue contrast, such as MRI, is required. A device with this capability would be useful for adaptation to a flexible endoscope, for application to the gastrointestinal tract or inner arterial wall, and for assessment of the stiffness, texture, and presence of abnormal subsurface stiffnesses (such as tumorous lesions).

This paper outlines the development to date of a novel tactile sensing device to be used for *in-vivo* tissue stiffness measurements. The perceived benefits of such a device would be to provide the clinician with detailed diagnostic information that could be used to assess the health of tissues and primarily for the detection, localization, and characterization of suspected tumorous tissue, otherwise hidden during MIS. The device is to be MR compatible for the possibility of application with MRI guidance and combination with other MRI capabilities.

## 2 METHODOLOGY AND MATERIALS

### 2.1 Mechanical design

A device was required to perform 'palpation', the diagnostic technique used by clinicians to retrieve information about an anatomical feature by touch. This is generally achieved by using the fingertips and sometimes palms to impinge directly upon the surface using lateral motions to feel for changes in stiffness and texture. A surgeon can use this technique to identify the presence of abnormalities (such as hard lumps) hidden up to a few centimetres below the surface [**25**]. The device would be designed to allow force information to be retrieved (using sensors) from tissues out of range of standard digital

palpation and should be designed in a format similar to existing MIS tools.

The area of interest for this device was chosen to be the inner intestine, as discussions with surgeons revealed that it is often desirable to examine the health of the gut wall for the presence of cysts and hard lumps which may indicate the presence of tumours. Similarly the prostate is often examined in men over the age of 40 to screen for prostate cancer [**26**]. As the process of 'sensing' the tissue would be carried out remotely from the user by the force sensors in the device, the device must also be capable of allowing actuation of the sensors while at the point of application. As target identification, visualization, and guidance would be achieved using MRI, the device must also be MR compatible.

Generally, MIS tools are designed with long stiff handles that can be inserted, through small incisions approximately 1 cm in size, to the operating region within the body. The exact morphology of the device would be determined by the region of its intended application. The body of the device was made using plastics (epoxy resin using rapid prototyping fabrication), to achieve MR compatibility. The body was designed to be long and thin to allow insertion through the anus and manoeuvring to the region of interest. Guidance would be achieved by MRI through the use of fiducial markers [**27**] that are to be implemented at a future date.

The design includes an actuating tip to allow sensors to be moved laterally across the tissue surface (Fig. 1). The actuation occurs in one plane and is achieved using a series of mechanical links, with two pairs of antagonistic nylon actuation cables connected to the distal link; the working envelope of this is shown in Fig. 1(b). The exact nature of the bending is dependent on the relative stiffness of the joints and relative tensions of the cable pairs, but this can be controlled to allow the distal link to begin bending first. This effect becomes more difficult to control with a larger number of links as weight becomes an issue and thus tensions must be greater; the preload tension required in this design is approximately 15 N for the distal link and 10 N for the proximal link. This design incorporates two links with a length of 76 mm and has a diameter of 12 mm, leading to a resemblance of the human finger.

The device was designed to allow control using a hand-operated controller. This controller was also fabricated using rapid prototyping and incorporates a tensioning mechanism and control wheels geared down with a plastic 4:1 planetary gearbox (Fig. 2). The controller also includes a clutch mechanism

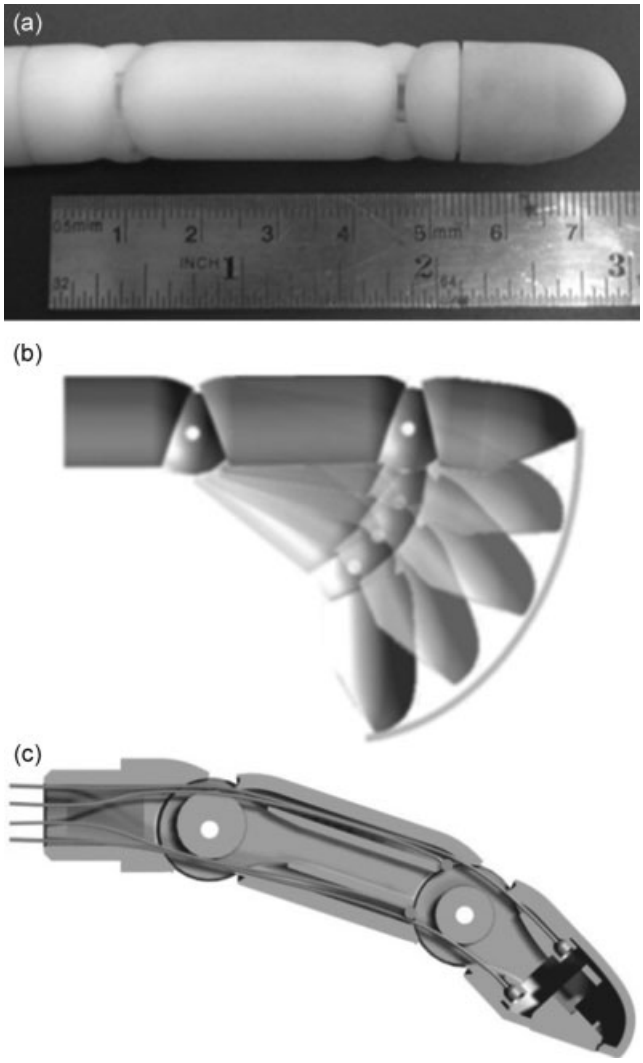


**Fig. 1** (a) The realized palpation device fabricated using rapid prototyping. (b) The single plane working envelope of the actuated device. (c) Computer aided design (CAD) drawing showing the internal structure with actuation cables showing the position of the sensing tip

that allows the device to be controlled using both actuating cable pairs, or a single pair to allow one link to flex passively. The device is adaptable to allow connection to custom-designed air motors through the wheel axis; this allows a control program to be implemented for accurate positioning [**28**].

### 2.2 Characteristics of the sensor

The symbols used in this section are defined in Table 1.

The sensing device is to be used as a method for conveying touch information about a target tissue by examination of an area and development of a two-

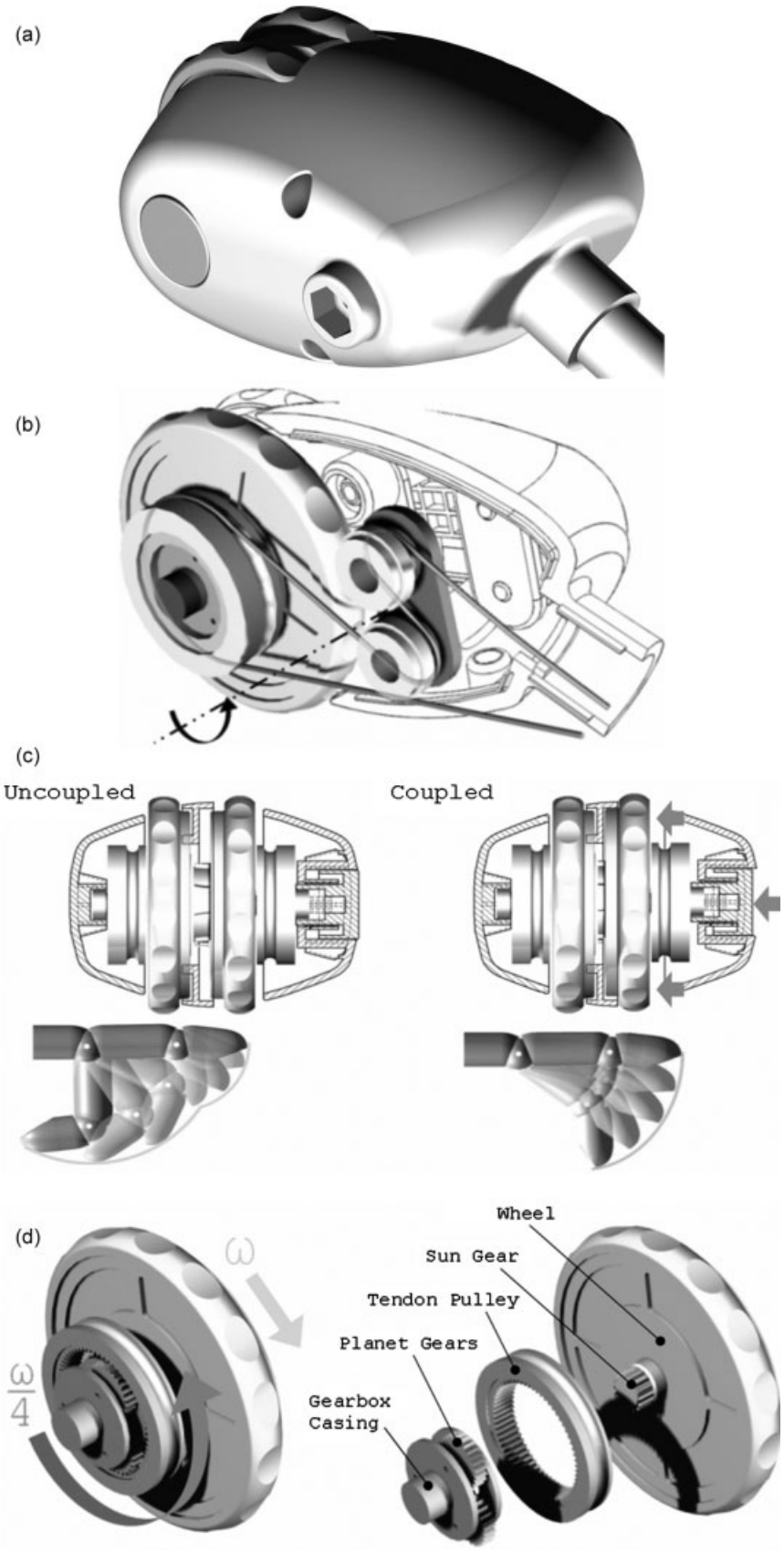


**Fig. 2** (a) CAD illustration of the complete controller. (b) Internal details showing the control wheel, gearing, and tensioning system. (c) Uncoupled and coupled clutch system which affects the method of actuation. (d) Detail of the planetary gearing system

**Table 1** Symbols used in this section

| Symbol | Explanation |
|---|---|
| $a_o$ | Output acceleration |
| $a_b$ | Base (exciting) acceleration |
| $f_n$ | Natural frequency |
| DC | Static value (0 Hz) |
| $V_s$ | Sensor output voltage |
| $H(s)$ | Transfer function in the $s$ domain |
| $R_1$, $R_2$, $R_3$, $R_4$ | Resistances used in the feedback circuit of the charge amplifier |
| $R_s$ | Sensor resistance |
| $C_c$ | Cable capacitance |
| $C_f$ | Feedback capacitance |
| $R_f$ | Output resistance in the feedback circuit |
| $C_2$ | Capacitance in feedback circuit |
| $C_s$ | Sensor capacitance |
| $Z_R$ | Ratio of parallel resistance of $R_f$ and $R_4$ to the total resistance of $R_f$, $R_4$, and $R_3$ |

dimensional stiffness profile. This force information can be fed back and potentially be represented to the user graphically or mechanically. To complete the haptic feedback loop, the operator can affect the location of assessment by moving the hand or finger in the same way that they would if carrying out regular 'palpation' techniques. The requirements of the task depend greatly on the area of application but, for general-purpose palpation, the sensitivity, resolution, range, and bandwidth are limited only by the operator's capabilities [**25**].

To define the task more definitely, a study of haptic and medical factors was undertaken. Table 2 has been compiled from a study of the literature [**29–31**]. In addition to these requirements, the general requirements of MR compatibility are also required as discussed above. The specification for compatibility of a device being used within the imaging volume (as the sensing device would need to be) is that the device is MR safe and does not significantly affect imaging quality. The generally accepted quantity here is that the SNR reduction is within 10 per cent [**12**] and that any image artefact or geometric distortion by the device should be quantified.

The sensor type selected for this work is piezoelectric. Piezoelectric sensors possess excellent compatibility material-wise and in operation; they are also highly dimensionally scalable and low cost (typically around £1 per sensor of 15 mm × 2 mm × 0.5 mm). These are advantages over MR-compatible sensors that have been used in other research. Piezoelectric sensors produce extremely low currents, in the range of nanoamperes, instead outputting charge, meaning that electromagnetic fields generated by them are of much lower magnitude than traditional sensor types, thus causing less interference. In terms of performance the sensors can be used over wide frequency and force ranges and because of their high stiffness also have high force resolution [**32**].

There are several challenges associated with using piezoelectric sensors. A major drawback is that they cannot be used to measure static forces; their capacitive nature leads to behaviour analogous to a high-pass filter, as shown in Fig. 3. Another problem is that their extremely high impedance (greater than 100 MΩ) means that it is difficult to use them directly linked to a measuring device as this causes charge to be drawn and hence the reading to become unreliable. Piezoelectric sensors are normally used by coupling with extremely high-impedance metal–oxide–semiconductor field-effect transistor circuits or charge amplifiers. Figure 4 depicts a piezoelectric sensor that is adapted for use in this work; the natural frequency $f_n$ of this sensor is determined to be 475 Hz.

### 2.3 Signal conditioning and data transmission

Where the output signal of a piezoelectric sensor will be comparatively low, it must be processed by a special high-input-impedance amplifier known as a charge amplifier. A charge amplifier allows the charge output to be measured without allowing a significant current to be drawn, which would immediately cause the actual measurement value to deteriorate.

A charge amplifier was designed to cause the passband of the high-pass filter to be as low as

**Table 2** Values of human touch sense capabilities and tumour characteristics derived from literature. The tumour stiffnesses given are averages for fibroadenoma and lobular carcinoma

| | | | |
|---|---|---|---|
| Tissue elastic modulus estimation | 90 kPa* | Fingertip point perception | ≈1–2 mm (given by the two-point limen) |
| Tumour elastic modulus estimation | 400 kPa* | Force resolution | ≈ 0.1 N [**30**] |
| Appoximate tumour size | 0–40 $cm^2$ (0–2 $cm^2$ being typical) | Maximum perceivable forces | 20 N at 0 Hz<br>1 N at 10 Hz |
| | | Maximum frequencies for force change perception | 5–10 kHz (texture shear force perception)<br>0–100 Hz (static forces) [**30**] |

*Estimations, as tissue stiffness is non-linear [**29**].

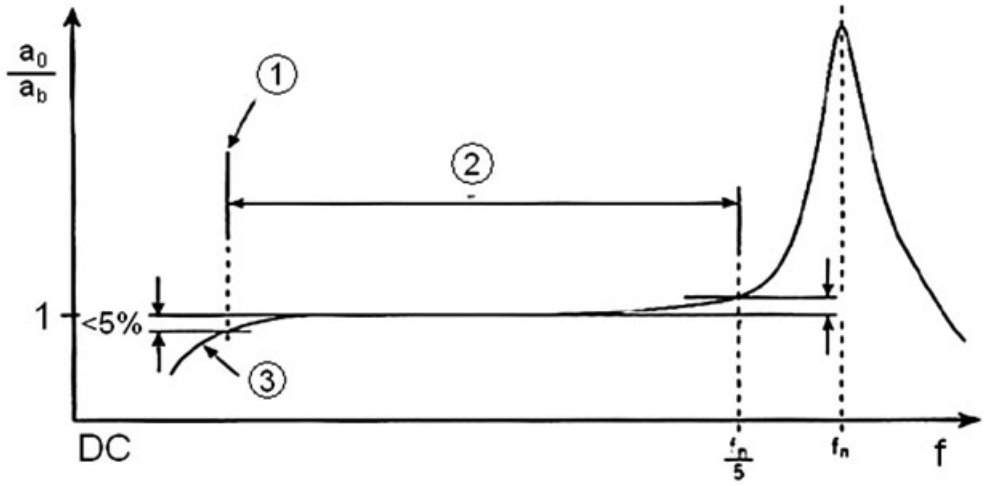


**Fig. 3** Frequency-dependent characteristics of piezoelectric sensors: ① low cut-off frequency; ② linear operating range; ③ output amplitude roll-off as first-order high-pass filter. (Adapted from reference [**32**])

possible to allow quasi-static force measurements. The charge amplifier in Fig. 5 implements a second-order high-pass function, with two poles and two zeros that set the cut-off frequency. The circuit includes a voltage integrating capacitance $C_f$, which determines the gain of the system, and a feedback operational amplifier circuit which acts as a parallel inductance–resistance circuit, giving a second-order system. With an extremely-high-output impedance the circuit will draw charge away slowly from $C_f$, preventing its saturation, and by carefully choosing the values of $R_f$, $R_4$, and $R_3$, the cut-off frequency can be adjusted. For very-low-frequency operation, low-noise low-bias-current operational amplifiers are selected with complementary metal–oxide-semiconductor inputs. The transfer equation of the entire system (charge amplifier and piezoelectric sensor) is given later in equation (3) and is derived below.

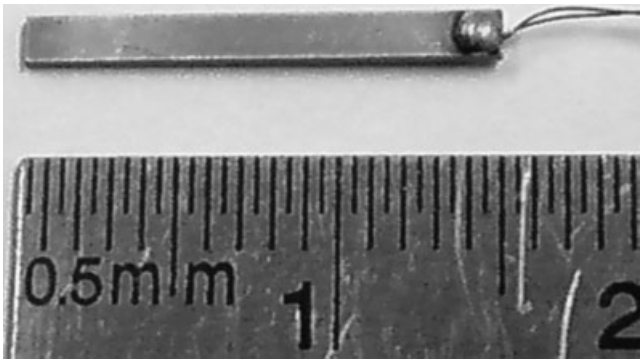


**Fig. 4** Piezoelectric bimorph adapted for use in this work

In this equation the sensor resistance and cable capacitance are omitted as the real values are such that they do not have any significant effect on the output ($R_s \approx 500\,\text{M}\Omega$; $C_c \approx 40\,\text{pF}$). Additionally, in the real design, the resistances $R_2$ and $R_1$ are equivalent; the following derivation follows these assumptions.

Looking at the currents at node A (by Kirchoff's current law)

$$i_1 + i_2 = -i_3 \tag{1}$$

The gain of the operational amplifier in the feedback circuit (within the dashed rectangle in Fig. 5) is derived as

$$\frac{V_i}{R_1} = -\frac{V_o}{(1/sC_2)+R_2}$$
$$\frac{V_o}{V_i} = -\left(1+\frac{1}{s\,R_2C_2}\right) \quad \text{(assuming that } R_2 = R_1\text{)} \tag{2}$$

The voltage across $R_f$ is related to the output of the feedback operational amplifier by the potential divider network of $R_f$, $R_4$, and $R_3$. The equivalent resistance of this is referred to as $Z_R$. Substituting equation (2) into equation (1) gives

$$C_s s V_s + \frac{V_o[-1-(1/sR_2C_2)][R_f \| R_4/(R_3+R_f\|R_4)]}{R_f}$$
$$= -C_f s V_o$$

Rearranging and substituting potential divider network for $Z_R$

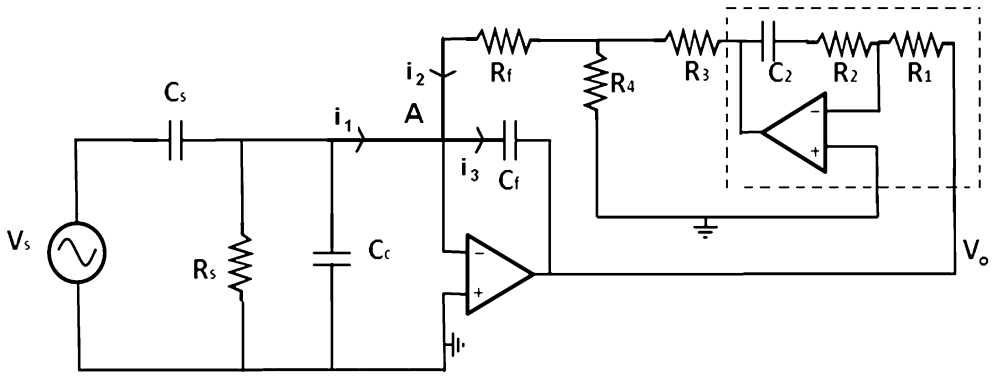


**Fig. 5** Charge amplifier and piezoelectric transducer equivalent circuit

$$C_s s V_s = -V_o \left[ sC_f + \frac{[-1-(1/sR_2C_2)]Z_R}{R_f} \right]$$

Further rearrangement yields the second-order transfer function $H(s)$ of the system according to

$$-\frac{V_o}{V_s} = \frac{sC_s}{sC_f + [-1-(1/sR_2C_2)](Z_R/R_f)}$$

$$H(s) = -\left( \frac{s^2 R_2 R_f C_2 C_s}{s^2 R_2 R_f C_2 C_f - sR_2 C_2 Z_R - Z_R} \right) \quad (3)$$

**Table 3** Component values used for this device

| Parameter | Value |
|---|---|
| $C_s$ | 500 pF |
| $C_c$ | 40 pF |
| $R_s$ | 500 MΩ |
| $C_f$ | 1 nF |
| $R_f$ | 100 MΩ |
| $R_1$ | 620 kΩ |
| $R_2$ | 620 kΩ |
| $R_3$ | 100 kΩ |
| $R_4$ | 10 kΩ |
| $C_2$ | 5 μF |

The component values given in Table 3 give a cut-off frequency of 1 Hz and a passband gain of 0.5.

This is a high-impedance system and can act as an antenna within the noisy MRI environment, as the r.f. radiation component can induce a potential difference between the sensor conductor wires. The scheme for data transmission and noise elimination shown in Fig. 6 is proposed. Cables connected from the control room to the scanner room constitute potential antennae inducing and amplifying noise; therefore an optical fibre is used for data transmission and all electrical pulses are encoded by optical converters into optical pulses. The sensor array is connected to the charge amplifier system and through to the data acquisition device with shielded twisted cables connected to the ground of the scanner. All electronics in the scanner room are placed in a Faraday cage.

### 2.4 Sensing methodology

The piezoelectric sensors have been shown to produce an output when actuated using a 'sliding scheme', whereby the sensors are indented a constant depth into a soft substrate and moved linearly across (Fig. 7). The sensors are to be used to build up

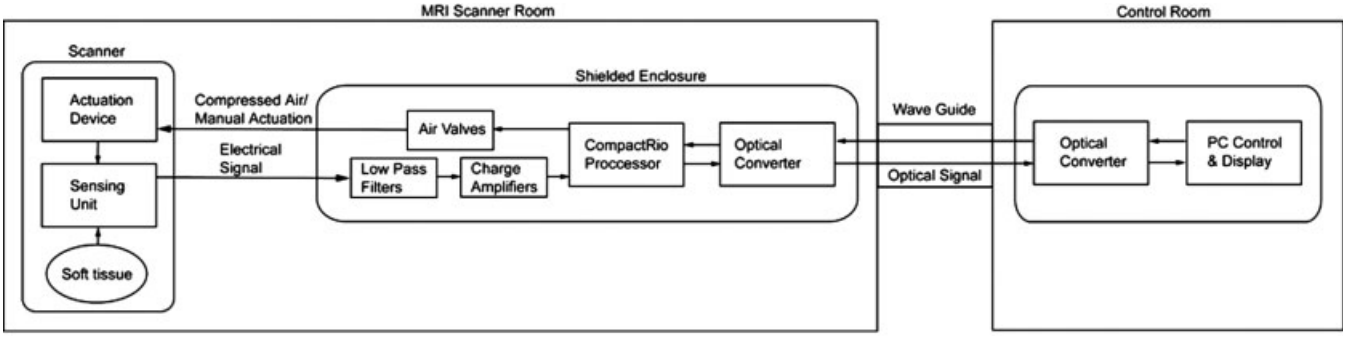


**Fig. 6** Proposed data transmission scheme for noise elimination (PC, personal computer)

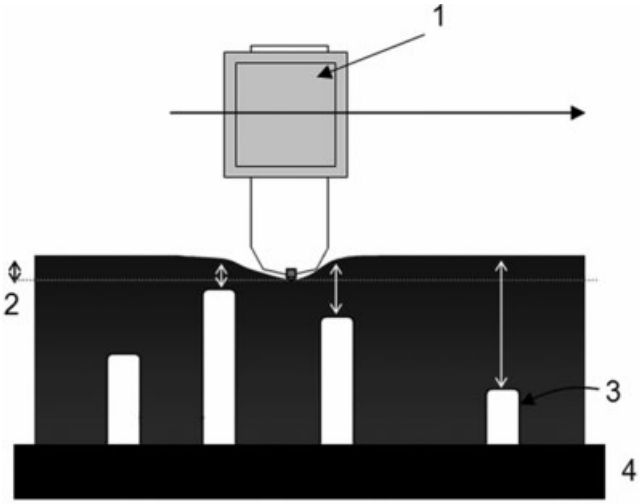


**Fig. 7** Concept of sliding actuation scheme. The single sensor is incorporated in a mount 1 and actuated linearly across a material surface at a constant indentation depth 2. Harder inclusions 3 are mounted on a hard base 4 and give different depths below the surface

two-dimensional stiffness profiles; however, as there is only one plane available for actuation, the one-dimensional output of a single sensor must be combined with the outputs of a series of adjacent sensors, to generate a two-dimensional contour (Fig. 8).

## 3 RESULTS AND DISCUSSION

### 3.1 MR compatibility tests

Experiments were carried out to determine the MR compatibility of the sensor in a 1.5 T Siemens Magnetom system. The sizes of the image artefacts were quantified using the ASTM F2119 protocol [**33**]. The piezoelectric sensor was disconnected and placed in a container of $CuSO_4$ solution. Scans were taken using gradient echo (GE) and turbo spin echo (TSE) image sequences, as shown in Table 4. The sizes of the artefacts were measured from the device boundary to the artefact edge; the maximum distance is taken.

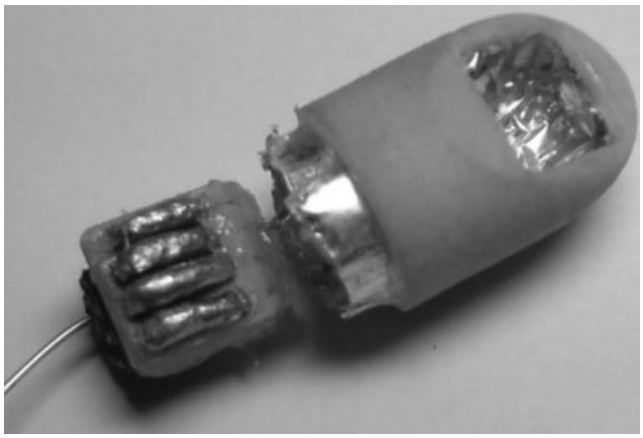

**Fig. 8** Sensing tip with four sensor contact points shown on the removed mount. Sensors are cut down to 5 mm length. The foil shield for electromagnetic interference suppression is also shown

The maximum artefact size was observed to be 2.2 mm × 18 mm in the GE image, which is slightly larger than the sensor body at 1.5 mm × 15 mm. This artefact size means that the sensor can be placed within the imaging volume without significantly distorting the image of interest; i.e. the position of the tumour relative to the tool will remain clear, and no significant distortion of the tissue will occur. The artefact produced under gradient echo is shown in Fig. 9.

MR safety was shown, as no appreciable force was measured with the sensor placed inside the scanner bore; from the literature, lead zirconium titanate has been determined to have a magnetic susceptibility of $-30\times10^{-6}$ or less. The test concludes that the sensor is non-magnetic [**34**].

### 3.2 Application within the MRI scanner room

An experiment was conducted to validate the concept by mounting the palpation device described in section 2.1 on an MR-compatible positioning robot (Fig. 10), developed in a previous study [**9**]. This robot is actuated using piezoceramic motors and can translate in three linear Cartesian directions. Air motors are attached to the palpation device to

**Table 4** Details of image sequences selected

| Sequence | Repetition time (ms) | Echo time (ms) | Flip angle (deg) | Number of slices | Thickness of slice (mm) | Spacing (mm) | Resolution | Field of view (mm) | Bandwidth (Hz/pixel) |
|---|---|---|---|---|---|---|---|---|---|
| TSE | 500 | 20 | 180 | 15 | 3 | 3 | 256×256 | 300 | 130 |
| GE | 200 | 15 | 30 | 15 | 3 | 3 | 256×256 | 300 | 130 |

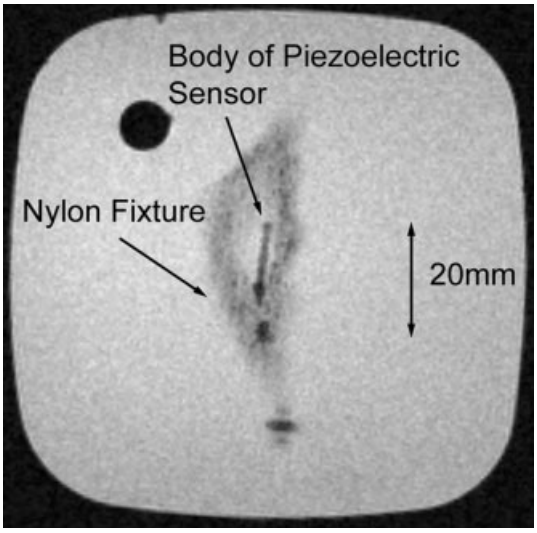


**Fig. 9** Sensor which is indicated in solution for measurement of the artefact

facilitate the actuation of the tip. The integrated system has been shown to cause a maximum SNR reduction of 9.5 per cent with a TSE sequence and 5.5 per cent with a GE sequence, occurring when all the joints are activated.

The output for the sliding sensing scheme of a sensor over a phantom soft-tissue model with a hard inclusion (Fig. 11(a)) indicates the result expected, a voltage peak at the position of the inclusion (Fig. 11(a)). However, although measures have been taken to counteract electromagnetic interference, it was found that a large degree of noise is imparted to the signal.

A further set of experiments was undertaken to determine the source of the noise. The unactuated sensor output was analysed by Fourier transform at several distances from the scanner, including when physically attached to the inner surface of the bore, while TSE and GE sequences were running, and when no sequence was running. It was found that all permutations of the experiment with the sensor mounted in such a way that it has no mechanical connection to the bore gave similar results, with the signal roughly approximating white noise of very low amplitude (Fig. 12(a)). However, signals from the sensor when attached to the inner surface of the scanner bore were noisy during either GE or TSE scanning. The Fourier transform of the noisy signals showed definite peaks at 10 Hz, 40 Hz, and most prominently at 100 Hz (Fig. 12(b)). It was concluded that the noise is imparted owing to mechanical vibration of the sensor transmitted through the mount. A fifth-order low-pass finite impulse response digital filter was applied to the acquired data and it was found that a cut-off frequency of 5 Hz was sufficient to improve the output waveform greatly. Figure 11(b) illustrates the effect of filtering on the signal in Fig. 11(a).

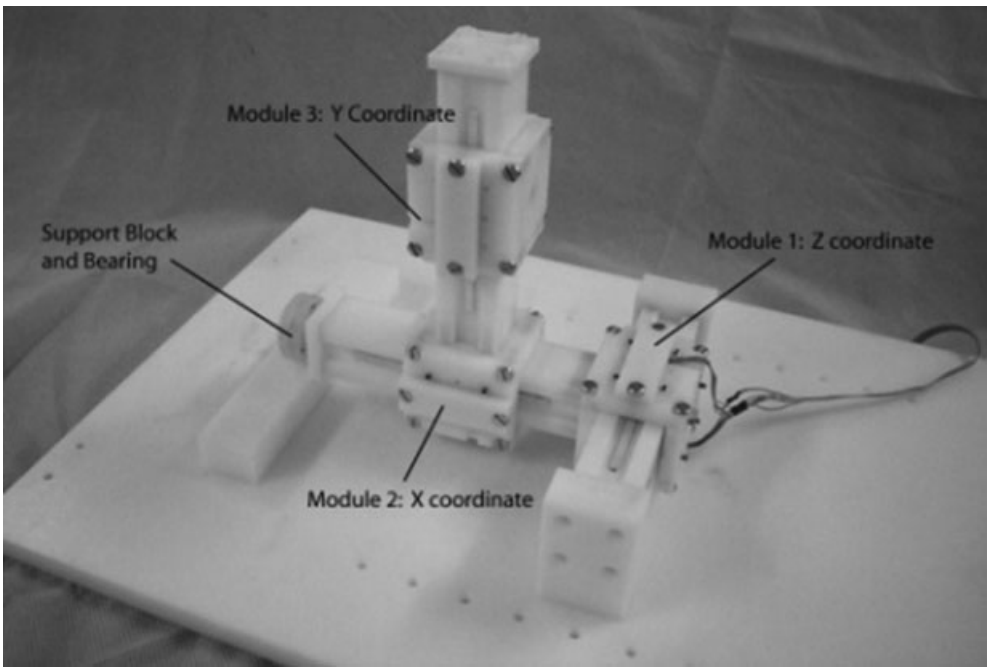


**Fig. 10** MR-compatible positioning robot developed by Elhawary *et al.* [**9**]

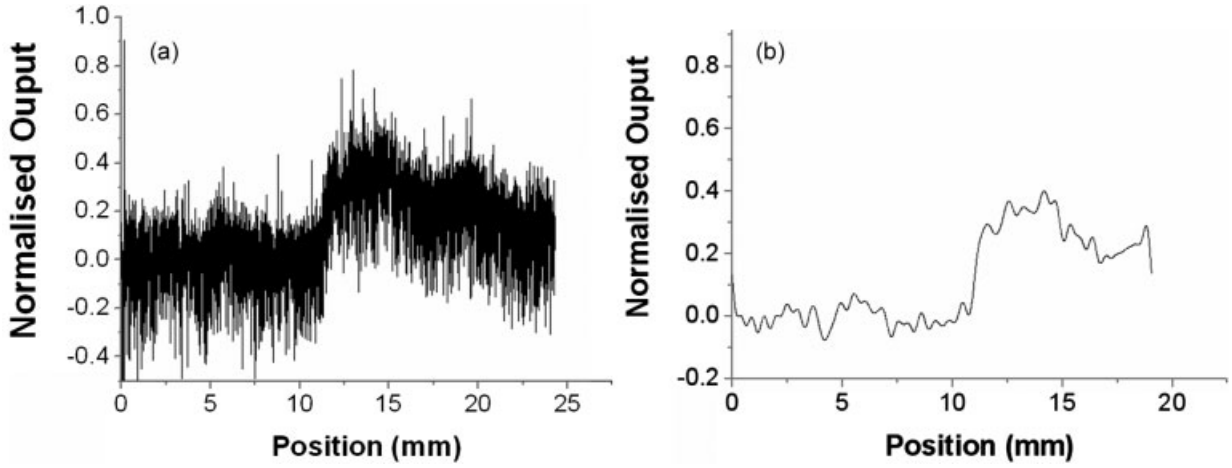


**Fig. 11** (a) Output of the sensor within the scanner during a GE scan, showing induced noise (inclusion depth, 3 mm; indentation depth, 1 mm). (b) Sensor output from (a) after application of a fifth-order low-pass finite impulse response filter with a cut-off frequency of 5 Hz, showing an inclusion position between 11 mm and 17 mm

### 3.3 Application and surface profiling

The palpation device described in section 2.1 with the four sensor tips (Fig. 8) affixed was actuated over a soft-tissue model (Fig. 13(a)), with a hard inclusion. This was achieved using identical test conditions and set-up with the previous experiments (section 3.2); therefore the inclusion depth was 3 mm and the indentation depth of the sensors was 1 mm. Actuation was controlled using air motors attached to the controller wheel axis, to give a predictable rate of motion. The sensor outputs were combined to produce the two-dimensional map of the material stiffness variation as shown in Fig. 13(b). It can be seen that a clear peak occurs between 10 mm and 16 mm when the sensors cross over the location of the inclusion.

## 4 CONCLUSIONS

It has been shown that the principle of force sensing within the MR scanner isocentre is achievable using piezoelectric force transducers although challenges arise from the presence of scanner-induced noise. It is conceivable that this noise can be removed by using just digital filtering alone, as the frequencies of the noise are well above the frequencies of useful information. However, as the noise has been shown to be almost entirely mechanical, it may also be possible to remove the noise by using a mechanical low-pass filter (damper) to decouple the scanner vibration from the sensor. It has been shown that it is possible to generate a two-dimensional map of voltage change due to stiffness variation of a soft-tissue model and to locate the position of a harder

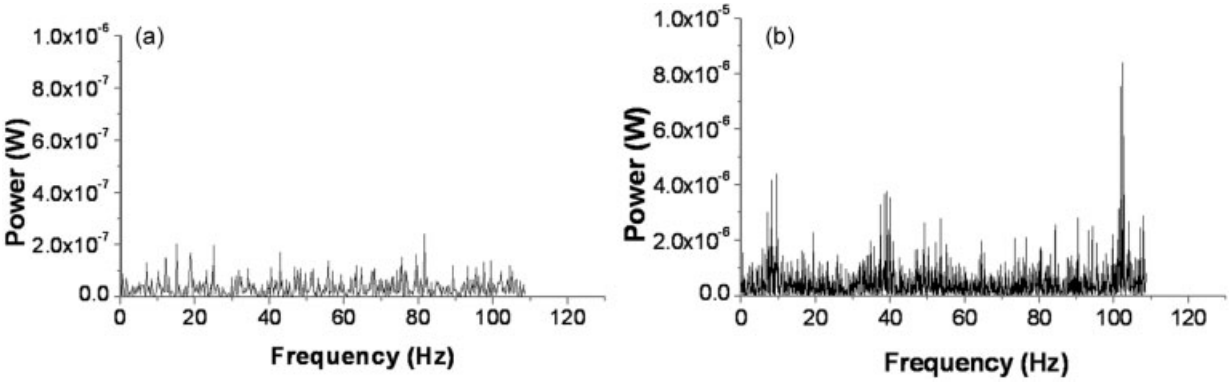


**Fig. 12** (a) Fourier transforms of sensor signals when unattached to the bore, at any distance and with any scan sequence (or none) show similar frequency patterns, with low magnitudes. (b) Fourier transform of sensor signal when attached to the scanner bore during any scan. Note the scale in (b) is ten times larger than in (a)

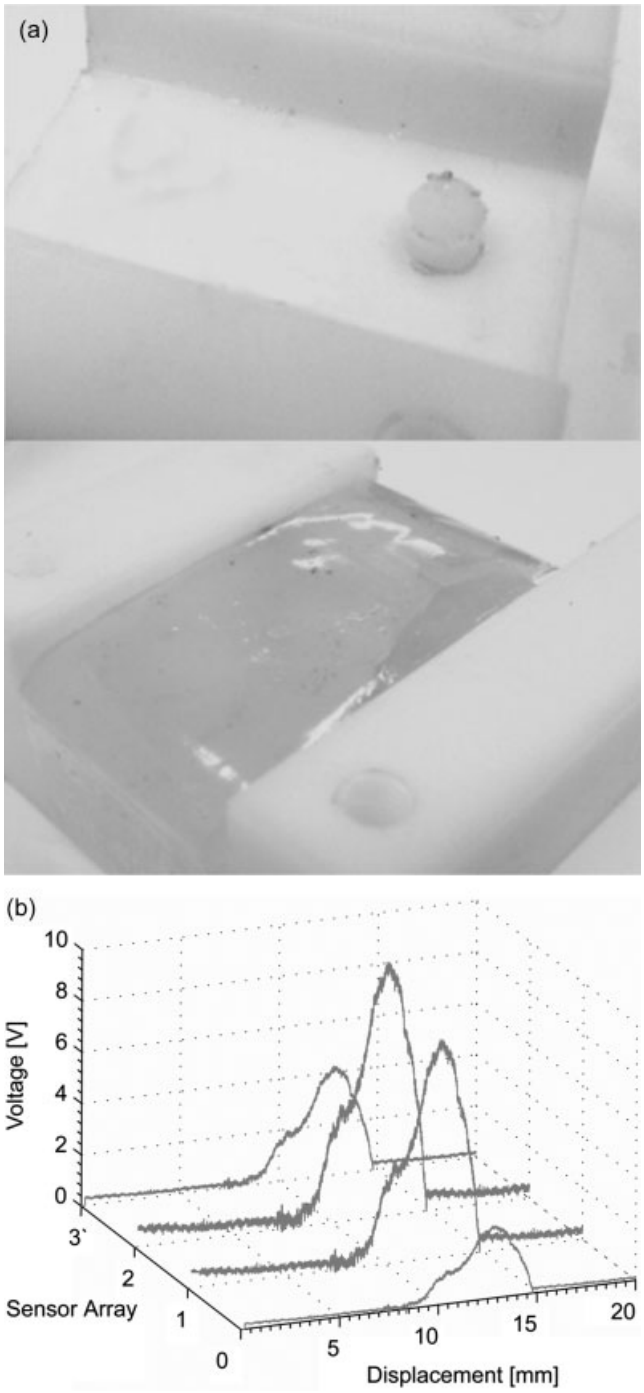


**Fig. 13** (a) Photograph of the phantom, showing soft poly(vinyl chloride) plastisol gel (Spenco™ 'Dermal Pad') material (bottom) overlying a harder plastic inclusion (top). (b) Two-dimensional stiffness map of the output voltage due to varying material stiffness. An inclusion is detected between 10 mm and 16 mm

subsurface inclusion by a mechanical action approximating palpation.

Future work involves more comprehensive characterization of the sensor output so that quantitative force measures may be achieved. Additionally, the full system must be thoroughly tested in operation within an MRI environment. Incorporation of this technology with fiducial markers would allow sensor position information to be retrieved from the scanner, such that sensor position may be mapped to the output. *In-vitro* soft-tissue experiments are required during scanning so that the system operation is fully verified.

## REFERENCES


1 **Mack, M. J.** Minimally invasive and robotic surgery. *Jama*, 2001, **285**, 568–572.
2 **Eltaib, M. E.** and **Hewit, J. R.** Tactile sensing technology for minimal access surgery – a review. *Mechatronics*, 2003, **13**, 1163–1177.
3 **Howe, R. D.** and **Matsuoka, Y.** Robotics for surgery. *A. Rev. Biomed. Engng*, 1999, **1**, 211–240.
4 **Virtanen, J.** *Enhancing the compatibility of surgical robots with magnetic resonance imaging*. PhD Dissertation, Faculty of Technology, University of Oulu, Oulu, Finland, 2006.
5 **McRobbie, D., Moore, E. A., Graves, M. J.,** and **Prince, M. R.** *MRI: from picture to proton,* 1st edition, 2003 (Cambridge University Press, Cambridge).
6 **Hempel, E., Fischer, H., Gumb, L., Hohn, T., Krause, H., Voges, U., Breitwieser, H., Gutmann, B., Durke, J., Bock, M.,** and **Melzer, A.** An MRI-compatible surgical robot for precise radiological interventions. *Computer Aided Surg.*, 2003, **8**, 180–191.
7 **Koseki, Y., Chinzei, K., Koyachi, N.,** and **Arai, T.** Robotic assist for MR-guided surgery using leverage and parallelepiped mechanism. In Proceedings of the Third International Medical Image Computing and Computer-assisted Intervention (*MICCAI 2000*), Lecture Notes in Computer Science, vol. 1935, Pittsburgh, Pennsylvania, USA, 2000, pp. 940–948 (Springer-Verlag, Berlin).
8 **Chinzei, K., Hata, N., Jolesz, F. A.,** and **Kikinis, R.** Surgical assist robot for the active navigation in the intraoperative MRI: hardware design issues. In Proceedings of the 2000 IEEE/RSJ International Conference on *Intelligent robots and systems* (*IROS 2000*), Takamatsu, Japan, 2000, pp. 727–732 (IEEE, New York).
9 **Elhawary, H., Zivanovic, A., Rea, M., Davies, B. L., Besant, C., McRobbie, D., Souza, N. D., Young, I.,** and **Lamperth, M.** A modular approach to MRI compatible robotics: interconnectable one DOF stages. *IEEE Engng Medicine in Biology Mag.*, 2008, **27**(3), 35–41.
10 **Stoianovici, D.** Multi-imager compatible actuation principles in surgical robotics. *Int. J. Medical Robotics Computer Assisted Surgery*, 2005, **1**, 86–100.

**11** ASTM F2503-05. *Standard practice for marking medical devices and other items for safety in the magnetic resonance environment*, 2005 (ASTM International, West Conshohocken, Pennsylvania).

**12 Chinzei, K., Kikinis, R.,** and **Jolesz, F. A.** MR compatibility of mechatronic devices: design criteria. In Proceedings of the Second International Conference on *Medical image computing and computer-assisted intervention* (*MICCAI 99)*, Lecture Notes in Computer Science, vol. 1679, Cambridge, UK, 1999, pp. 1020–1030 (Springer-Verlag, Berlin).

**13 Burdet, E., Gassert, R., Gowrishankar, G., Chapuis, D.,** and **Bleuler, H.** fMRI compatible haptic interfaces to investigate human motor control. In Proceedings of the International Symposium on *Experimental robotics* (*ISER 2004*), Singapore, 2004, pp. 25–34 (Springer-Verlag, Berlin).

**14 Tada, M.** and **Kanade, T.** Design of an MR-compatible three-axis force sensor. In Proceedings of the 2005 IEEE/RSJ International Conference on *Intelligent robots and systems* (*IROS 2005*), 2005, pp. 3505–3510 (IEEE, New York).

**15 Moser, R., Gassert, R., Burdet, E., Sache, L., Woodtli, H. R., Erno, J., Maeder, W.,** and **Bleuler, H.** An MR compatible robot technology. In Proceedings of the 2003 IEEE International Conference on *Robotics and automation* (*ICRA '03*), Taipei, Taiwan, 2003, pp. 670–675 (IEEE, New York).

**16 Gassert, R., Chapuis, D., Bleuler, H.,** and **Burdet, E.** Sensors for applications in magnetic resonance environments. *IEEE/ASME Trans. Mechatronics*, 2008, **13**(3), 335–344.

**17 Sutherland, G. R., McBeth, P. B.,** and **Louw, D. F.** NeuroArm: an MR compatible robot for microsurgery. In Proceedings of the 17th International Congress and Exhibition on *Computer assisted radiology and surgery* (*CARS 2003*), International Congress Series, vol. 1256, 2003, pp. 504–508 (Elsevier, Amsterdam).

**18 Tse, Z. T. H., Elhawary, H., Zivanovic, A.,** and **Lamperth, M..** A one degree of freedom MR compatible haptic system for tissue palpation. In Proceedings of the 13th Annual Meeting of the British Chapter of the International Society for Magnetic Resonance in Medicine, 2007, paper 013 (BCISMRM, Birmingham, UK).

**19 Tholey, G., Pillarisetti, A., Green, W.,** and **Desai, J. P.** Design, development, and testing of an automated laparoscopic grasper with 3-D force measurement capability. In Proceedings of the International Symposium on *Medical simulation* (*ISMS 2004*), Lecture Notes in Computer Science, vol. 3078, 2004, pp. 38–48 (Springer-Verlag, Berlin).

**20 Shostek, S., Ho, C., Kalanovic, D.,** and **Schurr, M. O.** Artificial tactile sensing in minimally invasive surgery – a new technical approach. *Minimally Invasive Therapies Allied Technologies*, 2006, **15**(5), 296–304.

**21 Dargahi, J.** and **Najarian, S.** An endoscopic force–position sensor grasper with minimum sensors. *Can. J. Electl Computer Engng*, 2003, **28**(3), 155–161.

**22 Rosen, J., Hannaford, B., MacFarlane, M. P.,** and **Sinanan, M. N.** Force controlled and teleoperated endoscopic grasper for minimally invasive surgery – experimental performance evaluation. *IEEE Trans. Biomed. Engng*, 1999, **46**(10), 1212–1221.

**23 Madhani, A. J., Niemeyer, G.,** and **Salisbury, J. K.** The black falcon: a teleoperated surgical instrument for minimally invasive surgery. In Proceedings of the 1998 IEEE/RSJ International Conference on *Intelligent Robots and Systems* (*IROS '98*), Victoria, Canada, 1998, pp. 936–944 (IEEE, New York).

**24 Rizun, P. R., Gunn, D. C., Cox, B. L.,** and **Sutherland, G. R.** Mechanical design of haptic forceps for robotic surgery. in Proceedings of the Symposium on *Haptic interfaces for virtual environment and teleoperator systems*, Arlington, Virginia, USA, 2006, pp. 331–335 (IEEE, New York).

**25 Field, D.** *Anatomy: palpation and surface markings,* 2nd edition, 1997 (Butterworth–Heinemann, Oxford).

**26 Bryant, R. J.** and **Hamdy, F. C.** Screening for prostate cancer: an update. *Eur. Urology*, 2008, **53**(1), 37–44.

**27 Rea, M., McRobbie, D., Elhawary, H., Tse, Z. T. H., Lamperth, M.,** and **Young, I.** System for 3-D real-time tracking of MRI-compatible devices by image processing. *ASME/IEEE Trans. Mechatronics*, 2008, **13**(3), 379–382.

**28 Elhawary, H., Zivanovic, A., Rea, M., Tse, Z. T. H., McRobbie, D., Young, I. R., Paley, M., Davies, B.,** and **Lamperth, M.** An MR compatible mechatronic system to facilitate magic angle experiments *in-vivo*. In Proceedings of the Tenth International Conference on *Medical image computing and computer-assisted intervention* (*MICCAI 2007*), Lecture Notes in Computer Science, vol. 4792, Brisbane, Australia, 2007, pp. 604–611 (Springer-Verlag, Berlin).

**29 Wellman, P. H., Howe, R. D., Dalton, E.,** and **Kern, K. A.** Breast tissue stiffness in compression is correlated to histological diagnosis. Technical Report, Harvard BioRobotics Laboratory, Harvard University, 1999.

**30 Burdea, G.** *Force and touch feedback for virtual reality*, 1996 (John Wiley, New York).

**31 Dargahi, J. S. N.** Human tactile perception as a standard for artificial tactile sensing – a review. *Int. J. Med. Robotics Computer Assisted Surg.*, 2004, **1**, 23–35.

**32 Kistler, I. C.** The piezoelectric effect, theory, design and usage, 2007, available from http://www.designinfo.com/kistler/ref/tech_theory_text.htm.

**33** ASTM F2119-07. Standard test method for evaluation of MR image artifacts from passive implants, 2007 (ASTM International, West Conshohocken, Pennsylvania).

**34 Grimes, C. A.** High-frequency, transient magnetic susceptibility of ferroelectrics. *J. Appl. Physics*, 1996, **80**, 4548–4552.